UC Berkeley
UC Berkeley Previously Published Works

Title

Fuel-Cell Catalyst-Layer Resistance via Hydrogen Limiting-Current Measurements

Permalink

https://escholarship.org/uc/item/4vd402sc

Journal

Journal of The Electrochemical Society, 166(7)

ISSN

0013-4651

Authors

Schuler, Tobias
Chowdhury, Anamika
Freiberg, Anna T
et al.

Publication Date

2019

DOI

10.1149/2.0031907jes

Peer reviewed

Fuel-Cell Catalyst-Layer Resistance via Hydrogen Limiting-Current Measurements

Tobias Schuler,[1,=] Anamika Chowdhury,[1,2,=] Anna T. Freiberg,[1] Brian Sneed,[3] Franz B. Spingler,[1,*] Michael C. Tucker,[1] Karren L. More,[3,**] Clayton J. Radke,[2] and Adam Z. Weber[1,***,z]

[1]*Energy Conversion Group, Energy Technologies Area, Lawrence Berkeley National Laboratory, Berkeley, California 94720, USA*
[2]*Department of Chemical and Biomolecular Engineering, University of California, Berkeley, California 94720, USA*
[3]*Center for Nanophase Materials Sciences, Oak Ridge National Laboratory, Oak Ridge, Tennessee 37831, USA*

Significant mass-transport resistances in polymer-electrolyte-fuel-cell catalyst layers (CLs) impose a lower limit on Pt-loading levels, hindering wide-spread fuel-cell commercialization. The origin of this resistance remains unclear. Minimization of CL mass-transport resistance is imperative to achieve better CL design and performance. In this paper, an operando method based on H_2 limiting current is used to characterize and quantify CL resistance in traditional porous Pt/carbon-based electrodes. CL sub-resistances are isolated using continuum multiscale modeling and experiments, investigating the effects of reactant molecular weight, pressure, and ionomer to carbon weight ratio. The results expose CL resistance including both interfacial and transport components, although the majority of the CL resistance is ascribed to a local resistance close to the Pt reaction sites, which includes interfacial resistance and local transport resistance. Variations in temperature, humidity, and primary particle loading (Pt:C ratio) highlight the impact of operating conditions and CL design parameters on CL sub-resistances. The observed trends guide optimization of CL design to achieve novel low-loaded fuel-cell electrodes.

Commercialization of polymer-electrolyte fuel-cells (PEFCs) depends on reduction of costly metal content (typically Pt) in their catalyst layers.[1,2] Consequently, high performance at low Pt-loadings, defined as Pt mass per unit CL geometric area, must be realized. Unfortunately, low Pt-loaded CLs exhibit significant mass-transport resistance that limits performance, especially at the O_2 electrode.[34] The source of this resistance remains ambiguous. Amelioration requires an understanding of its origin.

Transmission electron microscopy (TEM) has been extensively utilized to develop 3-D mappings of the PEFC CLs.[5,6] CLs consist of agglomerated primary carbon particles with Pt catalyst nanoparticles, and coated by ionomer thin films. With TEM, however, it remains a challenge to resolve the very thin ($\sim$10 nm) ionomer thin-film coating the catalyst particles because of low contrast against carbon. Recently, Lopez-Haro, et al.[7] used high-angle annular dark-field scanning transmission electron microscopy (HAADF-STEM) to study Cs^+-stained ionomer thin films on Pt-free carbon particles. Other techniques to map the ionomer and carbon phases include material sensitive and conductive atomic force microscopy (AFM)[8] and soft X-ray spectro-tomography (STXM).[9] In perhaps the most comprehensive study to date Cetinbas, et al.[10] used nano-scale X-ray computed tomography (nano-CT), TEM, and X-ray scattering combined with numerical reconstruction to report an ionomer thin-film distribution. Several studies have also highlighted the non-uniform distribution of ionomer in CL, with a significant fraction of Pt particles not in direct contact with ionomer phase.[11] As illustrated in Figure 1, these techniques establish that the CL consists of carbon aggregates ranging in the size 30 to 300 nm[12] covered by ionomer thin-film of thickness 5 to 30 nm.[10] These techniques, however, also highlight the heterogeneity in CL structure, which makes it difficult to isolate and quantify the pertinent mass-transport resistances.

Traditionally, CL mass-transport resistance is quantified from O_2-limiting current measurements, where the mass-transport limit is achieved using a dilute O_2 feed. Previous studies varied experimental and material parameters (e.g., pressure and Pt loading) to demonstrate that pressure and CL thickness have minimal impact on CL mass-transport resistance.[13–15] Conversely, ionomer content and Pt area do significantly impact CL performance.[12,13,15–17] These studies provide evidence that a local resistance close to the Pt particles is largely responsible for the high mass-transport resistance at low catalyst loadings.

Both modeling and experimental techniques have been employed to elucidate the origin of this local CL resistance. In one of the earliest works, Yoon and Weber[18] modeled oxygen transport through an ionomer film with individual Pt domains and observed a sharp increase in oxygen-transport resistance for very isolated domains. To agree with experimental data, they found that a more resistive ionomer film is required than anticipated from that of bulk ionomer. Debe[1] used kinetic-gas arguments to suggest that the low Pt-loading resistance is mainly due to frequency of collisions of reactant molecules with Pt, as this resistance is not seen for extended Pt whiskers without ionomer coating. Recent studies by Kongkanand, et al.[19,2] however, demonstrate that the high gas-transport resistance is also observed when Pt whiskers are coated by a thin film of ionomer, thus suggesting that the ionomer thin-film contributes to this resistance. Nonoyama, et al.[15] also came to a similar conclusion by characterizing CL transport resistance as a function of temperature and diluent-gas molecular weight (MW).

While the specific properties of the ionomer thin film in a CL remain elusive, model studies of thin films on planar substrates have been conducted. From grazing-incidence small-angle X-ray scattering (GISAXS),[20–23] X-ray reflectometry,[21,24] and transmission electron microscopy,[21] ionomer thin-film morphology is reported to be significantly different from that of bulk ionomer. Eastman, et al.[20] observed that water uptake and subsequent swelling are suppressed for films thinner than 60 nm accompanied by a decrease in effective water diffusion coefficient. They attributed chain confinement for the observed changes in material properties of the thin films. Similarly, Page et al.[25] observed a significant increase in elastic modulus of thin films as

---

[=]These authors contributed equally to this work.
[*]Electrochemical Society Student Member.
[**]Electrochemical Society Member.
[***]Electrochemical Society Fellow.
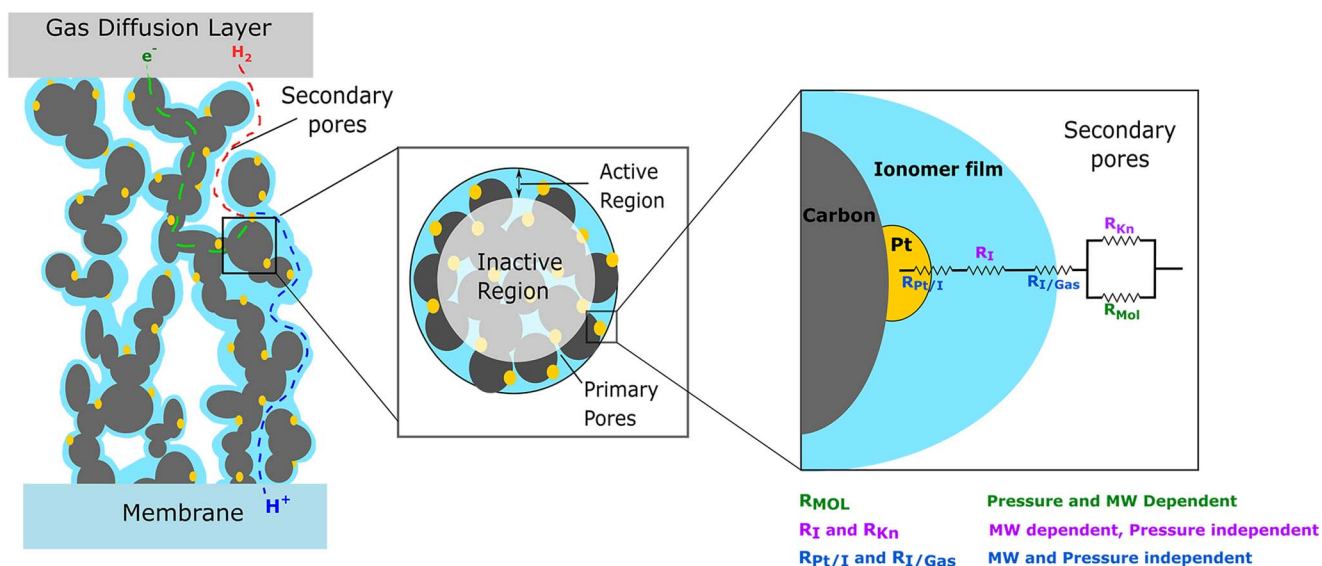[z]E-mail: azweber@lbl.gov

Figure 1. (Left) Qualitative illustration of reactant transport through the working electrode (WE). The reactant (red) diffuses through the pores, into and through the ionomer film (blue), and reacts at the Pt (yellow) catalyst site. Carbon particles are represented in black. (Center) Enlarged image of agglomerate coated by ionomer thin-film. The image highlights the active and inactive regions of the agglomerate at limiting current. (Right) The ionomer induced resistance includes of a series of ionomer and Pt nanoparticle interface resistances and permeation resistance within the ionomer thin-film. The gas-phase transport resistance in secondary pores is composed of both molecular and Knudsen transport.

compared to bulk ionomer and showed that stiffening could explain the reduced water uptake and transport rate. Other electrochemical properties such as proton conductivity have also been reported to be suppressed for ionomer thin-films. Siroma, et al.[26] measured lateral conductivity of recast ionomer films on Pt electrodes under humidified. In a more detailed study by Paul, et al.,[27] proton conductivity of thin films on Au electrode was examined as a function of operating conditions (temperature and relative humidity), film thickness and treatment conditions. Both studies report a thickness-dependent thin-film conductivity, with conductivity decreasing with decreasing film thickness at fuel-cell operating conditions. Kusoglu et al.[28] investigated the impact of ionomer equivalent weight (EW), defined as grams of dry polymer per mole ionic group. They concluded that EW plays a key role in inducing confinement-driven structural changes. For example, phase separation in thin films diminishes as the EW increases. The various observed morphological changes could give rise to low dissolved gas diffusivity in ionomer thin films compared to bulk ionomer. A recent review provides detailed discussion on ionomer thin films.[29]

Several studies also suggest the presence of an additional interfacial resistance, either at the gas/ionomer interface in the form of reactant-gas-dissolution resistance, or at the ionomer/Pt interface due to sulfonate-Pt interaction leading to catalyst poisoning.[16,30–32] Suzuki, et al.[33] modeled the CL with a gas-dissolution resistance at the gas/ionomer interface and compared against experimental results with good agreement. Among the initial few studies, Schmidt et al.[30] examined the impact of specifically adsorbing anions by studying oxygen reduction kinetics on rotating thin-film electrodes using liquid electrolytes with different anions. The electrode activity decreased consistently with increasing adsorption bond strength of anion on Pt. Similar findings have also been reported from rotating-disk-electrode (RDE) experiments. Subbaraman et al.[31] studied a range of Pt-catalyst surfaces in perchloric acid and Nafion mixtures using a RDE and observed a decrease in activity with increasing Nafion (ionomer) content. Shinozaki et al.[32] observed a significant increase in activity when perchloric acid was used as the proton conductor instead of Nafion. In a separate study using limiting-current measurements, Ono, et al.[16] reported higher local transport resistance with low EW ionomers, which could be due to higher density of sulfonic acid groups in low EW ionomers. Kodama et al.[34] observed better PEFC performance com-

pared to Nafion using a novel ionomer with sulfonamide groups. Density functional theory (DFT) further confirmed weaker adsorption of sulfonamide groups on Pt compared to sulfonic acid groups indicating that Pt poisoning by sulfonic-acid groups is a possible cause of high CL-transport resistances. Litster et al.[35] investigated thin-film transport using thin films cast on polycarbonate mesh substrates with no Pt (film thickness ∼50 nm). They did not observe a significant increase in mass-transport resistance as compared to bulk ionomer and attributed this to absence of Pt-sulfonate interactions. Recent studies by Kudo, et al.[36] and Jinnouchi, et al.[37] study gas transport through ionomer films on flat Pt electrodes to reveal an interfacial resistance at the ionomer/Pt interface.

As highlighted above, studies to date reveal a wide range of probable causes for high CL mass-transport resistance. A detailed discussion on this topic has been done by Weber and Kusoglu.[38] In this study, we use a H_2-pump, limiting-current apparatus to probe mass-transport limitations in PEFC CLs.[39] A H_2 pump presents an oxide-free surface, eliminates water production, and minimizes heat production, thus reducing local environment fluctuations. With a H_2-pump, Spingler et al.[39] observed a significant, unanticipated mass-transport resistance in a PEFC that they attributed to the CL. By varying reactant gas between H_2 and D_2, the CL resistance was subdivided into reactant square-root MW-dependent and MW-independent resistances. Diffusional processes and reactant transport through the ionomer thin film in the CL were believed the cause of the MW-dependent resistance, whereas MW-independent transport resistance was attributed to an adsorption or desorption process of sulfonate groups at the ionomer interface against Pt. Frieberg et al.[40] also used a H_2 pump setup to demonstrate that resistances derived from H_2-limiting currents can correct for H_2-air PEFC polarization behavior at low loadings, thereby providing confidence in this approach.

In the first section of this paper, we develop a continuum model of gas transport in a CL at limiting current to identify the possible sources of CL mass-transport resistance and expose the dependences of identified sub-resistances on pressure and reactant MW. This is followed by H_2-pump experiments to probe these dependences and quantify the various sub-resistances in CLs. The I:C ratio versus CL resistance study quantifies the individual sub-resistances and verifies the square-root MW dependence of transport resistances in CL. Impact of carbon support on CL morphology and Pt utilization is investigated
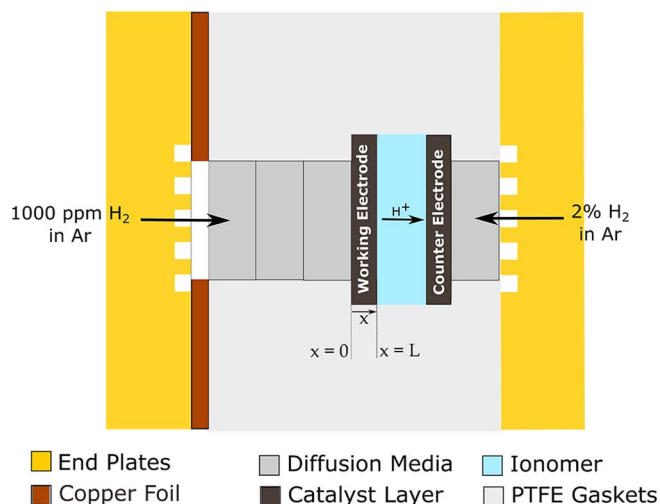
Figure 2. Experimental cell setup. MEA is sandwiched between GDLs. PTFE gaskets are used as electrical isolators between anode and cathode current collectors, for gas sealing and adjusting the compression rate. Cu foil on WE controlled the area of gas diffusion from flow channels to GDLs.

Figure 3. η as a function of a_v. The a_v corresponding to 20 and 50 wt-% primary particle loading is highlighted with dotted lines.

using different primary particle loadings supported by HAADF-STEM imaging.

Theory: Modeling Gas Transport in CL

To investigate the sources contributing to CL mass-transport resistance R_{CL}, a continuum 1-D model is used for the H_2-pump PEFC setup operating at limiting current, shown in Figure 2. With a dilute H_2 feed (1000ppm H_2 in Ar as used in this study), 1-D diffusion transport of reactant gas through the porous CL with reaction is modeled with governing equation

$$D_{CL}^{eff} \frac{d^2 C_{CL}(x)}{dx^2} - \frac{a_v i(x)}{nF} = 0 \qquad [1]$$

where $C_{CL}(x)$ is the local reactant gas concentration in the CL pores, x is the through-plane coordinate in the working electrode (WE), D_{CL}^{eff} is the effective reactant gas diffusivity through the CL pores given by reactant gas binary diffusivity in CL ($D_{H_2/Ar}$) corrected for CL porosity (ϕ) and tortuosity (τ): $D_{CL}^{eff} = \phi D_{H_2/Ar}/\tau$, a_v is the Pt area active at limiting current per unit CL volume, $i(x)$ is the local current density per unit Pt area, n is the moles of electrons transferred per mole of reactant gas (2), and F is Faraday's constant. Boundary conditions are fixed reactant gas concentration $C_{CL}(x = 0)$ at the gas diffusion layer (GDL)/CL interface ($x = 0$) and zero flux at the CL/membrane interface ($x = L$), where L is the thickness of the CL.

To estimate $i(x)$, the spherical-agglomerate model with simultaneous diffusion and reaction as illustrated in Figure 1 and described by Weber, et al.[41] is used. CL microstructure is modeled as agglomerates of porous carbon primary particles containing Pt nanoparticles and covered by a thin ionomer film.[42] Inter-agglomerate space is filled with water and/or ionomer. However, at limiting current, the reaction rate is much faster than the reactant mass-transport rate. The agglomerates thus have a high Thiele-modulus and a very low effectiveness factor.[41] In other words, any reactant that penetrates through the ionomer thin-film into the agglomerate will be immediately consumed upon collision with a Pt particle, of which there are many on the external agglomerate surfaces; thus, no reactant remains to diffuse into the interior of the agglomerate. Only Pt particles close to the external surface of the agglomerates are active; hence, the inter-agglomerate space does not significantly influence the generated limiting current. With these simplifications, the local limiting current density per unit
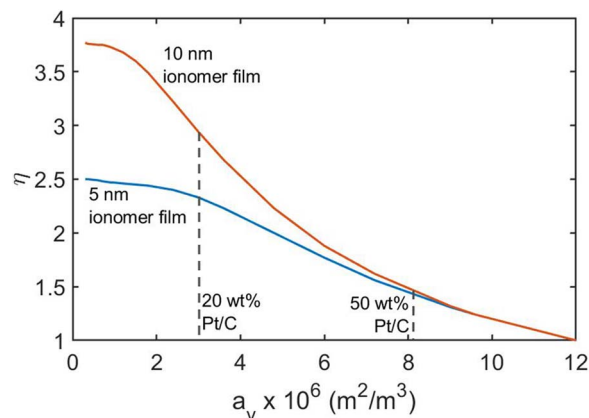
Pt area is written as[43]

$$\frac{i(x)}{nF} = \frac{\eta C_{CL}(x)}{R_{Local}} \qquad [2]$$

where R_{Local} is the local mass transport resistance close to Pt particles and η is a focusing factor defined as the ratio of reactant flux to discrete Pt particles to that of reactant flux to Pt particles idealized as forming a continuous surface with an equal total Pt surface area (refer SI). $C_{CL}(x)/R_{Local}$ specifies the 1-D mass flux to the Pt particles on the external agglomerate surface. However, Pt particles do not form a continuous surface, but occur as discrete patches. This leads to a greater 2-D flux to the Pt particles and is accounted for by correcting the 1-D flux, $C_{CL}(x)/R_{Local}$ by the focusing factor η. For a given agglomerate, η decreases with increase in Pt density since the ionomer/gas interface area per Pt particle on agglomerate external surface decreases. Large ionomer film thickness increases η because of greater reactant-collection area, i.e, the effective ionomer area from which a Pt particle draws reactant gas molecules. η is estimated from numerical simulations (details in SI) and shown in Figure 3 as a function of a_v.

Figure 1 highlights the possible contributions to R_{Local} encountered by reactant gases diffusing from the gas-occupied CL pores to the Pt particle surface. These resistances are (i) dissolution resistance at the gas/ionomer interface $R_{I/Gas}$; (ii) diffusional-transport resistance through the ionomer thin film R_I; and (iii) resistance due to catalyst interaction with sulfonate groups at the ionomer/Pt interface $R_{Pt/I}$. The sum of these three resistances close to Pt particles defines R_{Local}

$$R_{Local} = R_{I/Gas} + R_I + R_{Pt/I} = R_{I/Gas} + \frac{\delta}{\Pi_{gas}} + R_{Pt/I} \qquad [3]$$

where δ is ionomer thin-film thickness and Π_{gas} is ionomer thin-film reactant-gas permeability.

Solution of Equations 1 and 2 with attendant boundary conditions gives the reactant gas-concentration profile in the CL

$$C_{CL}(x) = \frac{C_{CL}(x = 0) \cosh(\alpha(x - L))}{\cosh(\alpha L)} \qquad [4]$$

where $\alpha = \sqrt{\eta a_v / R_{Local} D_{CL}^{eff}}$, is an inverse characteristic distance. The reactant concentration through CL is exponential, as highlighted by the hyperbolic term. We have shown in earlier studies that $\alpha L \ll 1$,[16,43] or $\cosh(\alpha L) \sim 1$. This leads to reactant concentration at $x = L$ (CL/membrane interface) approximately equal to the reactant concentration at the $x = 0$ (CL/GDL interface), providing a shallow concentration profile. This is later verified from experimental results as well.

To establish R_{CL} from Equation 4, the current density is expressed as

$$i_{lim} = \frac{nFC_{CL}(x=0)}{R_{CL}} = nFD_{CL}^{eff}\frac{dC_{CL}}{dx}\bigg|_{x=0} = nF\frac{C_{CL}(x=0)}{\frac{\coth(\alpha L)}{\alpha D_{CL}^{eff}}} \quad [5]$$

Equation 5 above represents reactant flux to the CL, multiplied by nF. The numerator of the rightmost term is the driving force for reactant transport from the GDL/CL interface ($x = 0$), where the reactant gas concentration is $C_{CL}(x = 0)$, to the Pt surface, where the reactant concentration is zero due to limiting current operation. The denominator thus gives $R_{CL} = \coth(\alpha L)/\alpha D_{CL}^{eff}$. Because $\alpha L \ll 1$,[16,43] using the first two terms of Taylor-series expansion of coth, we can thus express R_{CL} as

$$R_{CL} = \frac{L}{3D_{CL}^{eff}} + \frac{R_{Local}}{\eta a_v L} \quad [6]$$

The first term on the right side of Equation 6 is the through-plane mass-transport resistance in the CL, and the second term gives the total local resistance close to the ionomer-covered Pt particles, summed over all Pt particles. Equation 6 demonstrates that the total local resistance dominates at low loadings since L decreases with decreased loading (for undiluted electrodes where thickness is proportional to Pt loading). η and a_v remain constant for samples with constant primary particle loading (as mostly used in this study).[43]

Other resistances such as ohmic, kinetic, and channel flow are minimal at limiting current and hence neglected. Our previous work provides a detailed derivation of these results and also accounts for ionomer-film thickness and agglomerate-size distributions.[43] Ono et al. also obtained a similar result using a transmission-line model.[16] However, they did not subdivide R_{Local} into interfacial and transport components. Equations 6 is used in later sections to interpret the experimental results.

MW and pressure dependence of CL sub-resistances.—To quantify experimentally the sub-resistances in a PEFC CL, we examine the pressure and MW dependences of the terms in Equations 3 and 6. We first decompose D_{CL}^{eff} in Equation 6 into molecular and Knudsen contributions as they have different pressure and MW dependences. The Knudsen number for the gas-filled pores in PEFC CLs calculates to ~0.1 which is in the transition regime between Knudsen and molecular diffusion.[13] Using Bosanquet approximation, the effective diffusion coefficient becomes[44]

$$D_{CL}^{eff} = \frac{\phi D_{H_2/Ar}}{\tau} = \frac{\phi}{\tau}\left(\frac{1}{D_{H_2/Ar}^{Mol}} + \frac{1}{D_{H_2}^{Kn}}\right)^{-1} \quad [7]$$

where $D_{H_2/Ar}^{Mol}$ and $D_{H_2}^{Kn}$ are the reactant gas molecular and Knudsen diffusion coefficients through CL pores, respectively. Substitution of Equation 7 into Equation 6 gives

$$R_{CL} = \frac{L}{3}\frac{\tau}{\phi}\left(\frac{1}{D_{H_2/Ar}^{Mol}} + \frac{1}{D_{H_2}^{Kn}}\right) + \frac{R_{Local}}{\eta a_v L} \quad [8]$$

The first term on the right side of Equation 8, which represents molecular-transport resistance of the H_2 in Ar gas mixture, is both MW and pressure dependent according to Fuller-Schettler-Giddings equation[45]

$$D_{H_2/Ar}^{Mol} = \frac{0.0017\,T^{1.75}}{P\left(v_{H_2}^{1/3} + v_{Ar}^{1/3}\right)^2}\sqrt{\frac{1}{MW_{H_2}} + \frac{1}{MW_{Ar}}} \sim \frac{1}{P}\sqrt{\frac{1}{MW_{H_2}}} \quad [9]$$

where $D_{H_2/Ar}^{Mol}$ is in cm²/s, P is the total pressure in atmospheres, v is the species molecular volume in nm³, and T is the temperature in Kelvin. Conversely, the Knudsen-transport resistance of H_2, given by the second term in Equation 8, is only reactant MW dependent

(i.e., pressure independent)[45]

$$D_{H_2}^{Kn} = \frac{1}{3}d_p\sqrt{\frac{8RT}{\pi MW_{H_2}}} \propto \sqrt{\frac{1}{MW_{H_2}}} \quad [10]$$

where d_p is the pore diameter and R is the universal gas constant.

Lastly, we consider the contribution to R_{CL} from R_{Local} given by the third term on the right in Equation 8. From Figure 1, R_{Local} is composed of transport and interfacial components (see also Equation 3). The transport component (R_I) is given by the ratio of ionomer thin-film thickness (δ) to ionomer thin-film permeability of reactant gas (Π_{H_2}) (see Equation 3). Hydrated ionomer is known to phase-separate into aqueous and polymer-backbone rich domains; with the permeability of aqueous phase 10-fold greater than the polymer phase.[46] Reactant transport in a phase-separated ionomer thin-film occurs primarily through the aqueous phase. We thus use transport properties of water to model ionomer thin-film permeability, corrected for the water volume fraction as water transport properties are extensively reported in literature.

Gas permeability in water is defined as the product of diffusivity and partition coefficient. Within the low-pressure limit, the partition coefficient, defined as the inverse of Henry's constant, is pressure independent.[45] For the reactant gases used in this study (i.e., H_2 and D_2), Henry's constants in water are almost equal with less than a 10% difference.[47] Thus, the MW dependence of gas permeability is governed by reactant-gas diffusivity in water. Using modified Eyring activated state theory, Ferrell and Himmelblau[48] predicted diffusion of reactant species in water to scale as

$$\Pi_{H_2} \propto \Pi_{H_2/H_2O} = D_{H_2/H_2O}S_{H_2/H_2O}$$
$$D_{H_2/H_2O} \propto \frac{T}{\mu^\beta}\left[\frac{1+\Lambda^{*2}}{V_m}\right]^{0.6} \quad [11]$$

where Π_{H_2/H_2O} is H_2 permeability through water, D_{H_2/H_2O} is H_2 molecular diffusivity through water, S_{H_2/H_2O} is dimensionless H_2 partition coefficient defined as the ratio of H_2 concentration in gas phase to liquid phase, μ is water viscosity, $\beta = \sigma/(V_m/N_A)^{0.33}$, σ is the collision diameter in Lennard-Jones 6–12 potential, V_m is the molar volume of the gas at the normal boiling point, N_A is Avogadro's number, and T is absolute temperature. Λ^* is a dimensionless parameter given by $\lambda^* = h/\sigma(m\varepsilon)^{0.5}$, where h is Planck's constant, m is the mass of the diffusing molecule, and ε is the depth of potential well in Lennard-Jones 6–12 potential. For both H_2 and D_2, $\lambda^* > 1$.[49] As mentioned earlier, the partition coefficient of H_2 and D_2 are known to be equal;[47] the MW dependence of Π_{H_2/H_2O} can thus be approximated as

$$\Pi_{H_2/H_2O} \propto \frac{T}{\mu^\beta}\left[\frac{\Lambda^{*2}}{V_m}\right]^{0.6} \propto \left[\frac{1}{MW_{H_2}}\right]^{0.6} \sim \left[\frac{1}{MW_{H_2}}\right]^{0.5} \quad [12]$$

Assuming that all other parameters except MW in Equations 11 are equal for H_2 and D_2, the ratio of their permeabilities in water equals the square-root of the ratio of their MWs. A more rigorous derivation of this result is given in the SI.

Interfacial components of R_{Local} i.e., $R_{I/Gas}$ and $R_{Pt/I}$ are due to chemical processes such as dissolution kinetics of gas at the ionomer/gas interface and catalyst poisoning at the ionomer/Pt interface. Previous studies have shown that the local resistance R_{Local} is pressure independent.[15] Since the transport component R_I is also pressure independent as described above, we assert that the interfacial resistances must also be pressure independent. We further assume that the interfacial resistances are not functions of MW and are thus equal for H_2 and D_2 under the same operating conditions.[39]

From Equations 9, 10 and 12, all transport resistances in a CL scale with the square-root of reactant gas MW, whereas interfacial resistances are independent of reactant gas MW. We denote the fractional contribution of MW dependent transport resistances to R_{CL} as f_{MW}.

$$f_{MW} = \frac{\frac{L}{3}\frac{\tau}{\phi}\left(\frac{1}{D_{H_2/Ar}^{Mol}} + \frac{1}{D_{H_2}^{Kn}}\right) + \frac{R_I}{\eta a_v L}}{R_{CL}} \quad [13]$$

f_{MW} can be calculated by subtracting $R_{CL}^{H_2}$ from $R_{CL}^{D_2}$ and rearranging as follows (derivation presented in SI).

$$f_{MW} = \frac{R_{CL}^{D_2}/R_{CL}^{H_2} - 1}{\sqrt{MW_{D_2}/MW_{H_2}} - 1} \qquad [14]$$

Analogously, the pressure dependence of the transport resistance enables isolation of the resistance due to molecular diffusion in the CL as it is the only pressure-dependent one.

$$f_{Pressure} = \frac{\frac{L}{3}\frac{\tau}{\phi}\frac{1}{D_{H_2/Ar}^{Mol}}}{R_{CL}} = \frac{R_{CL}^{P_1}/R_{CL}^{P_0} - 1}{P_1/P_0 - 1} \qquad [15]$$

where $R_{CL}^{P_0}$ and $R_{CL}^{P_1}$ are the resistances at pressures P_0 and P_1, respectively.

Experimental

Cell assembly and operation.—As shown in Figure 2, the H_2 pump features an identical design to that of Hwang et al.[50] and Spingler et al.[39] The differential cell consisted of gold-plated parallel flow fields with 5 channels each of 0.4-mm width and separated by 0.2-mm wide ribs. The membrane electrode assembly (MEA) consisted of two CLs interposed by a Nafion NR212 membrane, used as received. The MEA was sandwiched between gas-diffusion layers (GDLs) (Sigracet 24BA, SGL, Wiesbaden, Germany) and the two flow fields. Reactant gases flow through parallel flow-field channels and diffuse perpendicularly through the GDLs and into the CL. The active cross-sectional area of the cell was determined by the CL area directly in contact with the GDL, while the remaining MEA area was covered by impermeable Teflon (PTFE) gaskets to prevent gas exposure. A Cu foil (0.04-mm thickness) with an aperture of 6.35 mm diameter limited the area over which diffusion from the channels to the GDLs occurred. Teflon gaskets (thickness ∼190 μm) seal the cell and achieve the desired GDL compression (strain) ratio of 0.8. Electrochemical impedance spectroscopy (EIS) was performed to ensure consistent ohmic resistances. Cell temperature was controlled with water recirculation through the endplates. Backpressure and humidity were controlled using a fuel-cell test station (Fuel Cell Technologies Inc., New Mexico, USA). The WE supply gas was bubbled through two external humidifiers connected in series for accurate humidity control of up to 90% relative humidity (RH). The first humidifier saturated the gas at a temperature above the target dew point and the second humidifier cooled the gas to the target temperature, condensing the excess moisture to achieve target RH with no droplets. Internal humidifiers of the fuel-cell test station were used to control RH for counter electrode (CE) gas line. As described below, cyclic voltammograms (CVs), EIS, and polarization curves were recorded using a Biologic VSP potentiostat (Seyssinet-Pariset, France).

Test protocol.—For the limiting-current measurements, a 2% H_2 in Ar mixture was utilized at the CE to minimize H_2 crossover and yet maintain a stable reference potential. Highly diluted reactant gases of 1000 ppm H_2 or D_2 in Ar were fed to the WE to achieve the mass-transport limit and minimize ohmic loses by limiting the maximum current generated. CE and WE flowrates were maintained at 200 and 500 cm^3/min (STP), respectively, for all measurements. A high stoichiometric flow at the CE minimized channel-flow resistance and provided a stable voltage reference.

The test procedure was as follows. The assembled cell was flushed using humidified Ar for 15 min. The CE gas feed was then switched to 2% H_2, and 50 cycles of cyclic voltammetry were performed by varying the WE voltage referenced to the CE from 0.08 V to 1.1 V at a scan rate of 50 mV/s. Finally, a constant potential of 0.35 V was applied on the WE (referenced to the CE). 1000 ppm H_2 or D_2 was fed on the WE and the total current density was recorded. A steady state was achieved within 3 to 5 minutes. Next, the current density induced by H_2 crossover from the CE was recorded by flowing Ar on the WE. The limiting-current density was estimated from the difference of total

Table I. Catalyst-layer compositions used in this study.

Sample #	Pt Loading (mg/cm^2)	I:C	Electrode Thickness (μm)
1	0.03	0.6	2.8
2	0.08	0.6	7.5
3	0.15	0.6	14.0
4	0.03	0.75	2.8
5	0.05	0.75	5.2
6	0.08	0.75	7.5
7	0.1	0.75	9.3
8	0.15	0.75	14.0
9	0.2	0.75	4.0
10	0.4	0.75	8.0
11	0.03	0.9	2.8
12	0.08	0.9	7.5
13	0.15	0.9	14.0
14	0.03	1.1	2.8
15	0.08	1.1	7.5
16	0.15	1.1	14.0
17	0.05	0.75	5.2
18	0.05	0.75	5.3
19	0.05	0.75	5.8

current density and crossover-current density. The common range of crossover and total current densities varied between 0.3 to 2.5 mA/cm^2 and 6 to 30 mA/cm^2, respectively. Other parameters varied include total gas pressure (1.0 and 1.7 bar absolute), WE reactant gas (H_2 or D_2), temperature (40, 60, 80°C), and RH (20 to 90%).

Samples.—Table I summarizes the membrane electrode assemblies (MEA) used in this study. Commercially available ionomer dispersions and membranes (DuPont DE2020CS, DuPont Nafion 212, Ion Power, Delaware, USA), and Pt-nanoparticle catalyst supported on high-surface area carbon (HSC) (TEC10E20E/ TEC10E30E /TEC10E50E from TKK, Tokyo, Japan) were used for electrode fabrication.[40]

MEA samples with various Pt loadings between 0.03 to 0.4 mg/cm^2 on the WE and constant primary particle loading of 20 wt% enabled a detailed Pt-loading study (samples 4 thru 10). The impact of pressure, temperature, RH, and reactant MW on CL resistance was also measured.

Impact of ionomer content was studied by varying the I:C ratio on WE from 0.6 to 1.1, referenced to the total carbon content, at different Pt loadings (sample 1 thru 4, 6, 8, 11 thru 13). Lastly, impact of primary particle loading was examined separately using samples with a constant total Pt loading of 0.05 mg/cm^2 and different primary Pt loadings varying between 20 to 50 wt% on the WE (samples 17 thru 19). HSC Ketjen black (KB) was used as filler to maintain constant electrode thickness of ∼5 μm and an I:C ratio of 0.75 referenced to the total carbon was used in these samples.

The CE in all the samples featured a constant Pt loading of 0.4 mg/cm^2 and I:C ratio of 0.75. The high-Pt mass loading coupled with high reactant flow rate ensured minimal mass-transport resistance at the CE.

ECSA measurements to estimate a_v.—As mentioned earlier, only a fraction of the total Pt particles are active at limiting current which constitute a_v. A large fraction of Pt particles in the interior of agglomerates remain inactive at limiting current operation. Currently, no experimental methods exist to determine a_v, the limiting-current active Pt area i.e, the area of Pt particles on the agglomerate external surface per unit CL volume. However, the ratio of external Pt particles (which constitute a_v) to the total Pt particles, denoted here as γ, is constant for samples with fixed primary particle loading,[43] provided that agglomerate size distribution, and agglomerate and CL porosity also remain constant. a_v is thus proportional to the electrochemically

active surface area (ECSA m^2 Pt) normalized by electrode volume with the proportionality constant γ (which is less than 1).

$$a_v L = \gamma \frac{ECSA}{A_{CL}} = \gamma r_f \qquad [16]$$

where A_{CL} is the electrode geometric area. ECSA normalized by the electrode geometric area ($ECSA/A_{CL}$) is commonly referred to as the roughness factor (r_f).[12] Padgett et al. estimated γ as 0.35 and 0.41 for HSC with primary particle loading 10 wt% and 50 wt% respectively. In our calculations, we use $\gamma \sim 0.365$ for 20 wt% particles, calculated from linear interpolation.

Writing R_{CL} in Equation 8 in terms of r_f yields

$$R_{CL} = \frac{L}{3} \frac{\tau}{\phi} \left(\frac{1}{D_{H_2/Ar}^{Mol}} + \frac{1}{D_{H_2}^{Kn}} \right) + \frac{R_{Local}}{\eta \gamma \ r_f} \qquad [17]$$

From Figure 3, $\eta \sim 2.5 - 2.9$ for ionomer film thickness 5 to 10 nm and $\gamma \sim 0.365$ as mentioned above. Thus, the product $\eta\gamma$ is of O(1).

H$_2$ adsorption underestimates ECSA for nanoparticles below 3.5 nm.[51] In addition, the low-H$_2$ current densities for the low Pt-loaded samples, which are comparable to the H$_2$ crossover current density, makes such analysis difficult. Therefore, ECSA was estimated from CO monolayer adsorption on Pt by CO stripping voltammetry.[52] The WE and CE were flushed using Ar for 5 mins. CE feed was then switched to 2% H$_2$ in Ar, and 20 cleaning cycles were performed between 0.08 to 1.10 V (referenced to CE) at a scan rate of 100 mV/s. The WE was, thereafter, fed with 1% CO diluted in Ar at 200 cm^3/min for CO adsorption for 5 mins. Next, Ar purged the WE at 200 cm^3/min (STP) for 25 mins to remove any excess CO and to obtain monolayer adsorption. Finally, three CVs were recorded by sweeping the WE potential between 0.08 to 1.10 V (referenced to CE) at a scan rate of 100 mV/s. ECSA was calculated from the charge integration of the CO peak. The 2nd and 3rd CVs served as a baseline for charge integration of the CO peak. A CO-monolayer oxidation charge of 420 mC/cm^2 was assumed in all the calculations.[53] All ECSA measurements were taken at 90% RH.

CL resistance estimation from GDL stacking method.—To compare against theory, R_{CL} from the GDL stacking method described by Spingler et al. [33] is used as a comparison. Total-cell resistance, R_{Total}, is experimentally determined from the ratio of average reactant feed concentration in the flow channels, C_{Avg}^{Feed} (averaged over channel length to account for the decrease in reactant concentration along the flow channels due to continuous diffusion loss into the CL), and the measured limiting-current density i_{lim} as

$$R_{Total} = \frac{nFC_{Avg}^{Feed}}{i_{lim}} \qquad [18]$$

R_{Total} is the total mass-transport resistance encountered by reactant gas diffusing from channel flow fields into the CL. Thus, R_{Total} for the H$_2$ pump in Figure 2 is

$$R_{Total} = NR_{GDL} + (R_{Foil} + R_{CL}) \qquad [19]$$

where R_{Foil} is the gas-phase transport resistance through the copper-foil aperture, R_{GDL} is the resistance of a single GDL, N is the number of GDLs stacked together, and R_{CL} is the CL resistance. In the GDL stacking method, R_{Total} is graphed as a function of N (sample plot presented in SI). The slope represents R_{GDL} and the intercept represents the sum of R_{Foil} and R_{CL}. R_{Foil} is equal to the foil thickness divided by the binary diffusion coefficient of H$_2$ in Ar (see SI for calculations). R_{CL} can thus be determined after subtraction of R_{Foil} from the measured intercept.

Scanning transmission electron microscopy.—Scanning transmission electron microscopy (STEM) and electron dispersive X-ray spectroscopy (EDS) characterization were performed using an FEI Talos F200X (Oregon, USA) operated at 200kV, which is optimized for high X-ray collection efficiency by the integration of four symmetrically arranged 30 mm^2 active-area silicon drift detectors within the
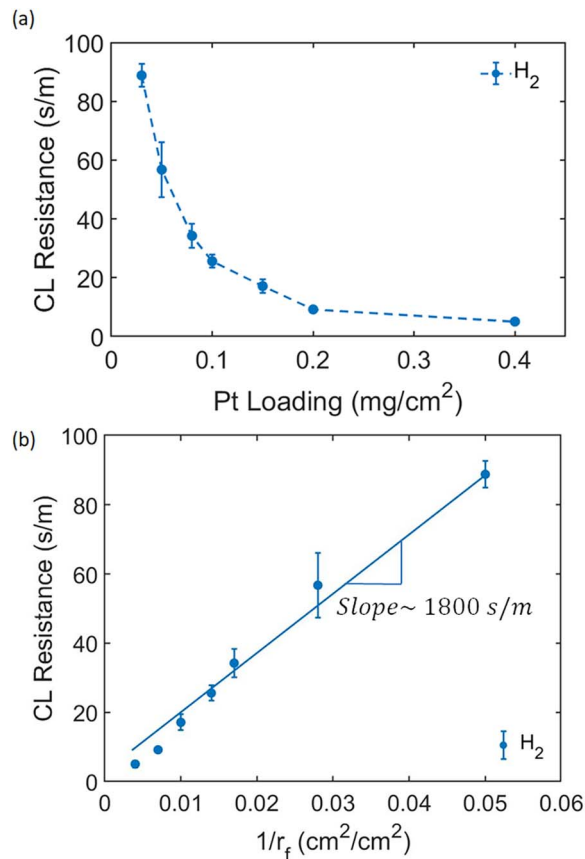

Figure 4. (a) Nonlinear decrease of CL resistance with increasing Pt loading, P = 1.03 bar, T = 40°C, RH = 90% (b) CL resistance as a function of $1/r_f$. The slope gives $R_{Local}/\eta\gamma$.

microscope column, resulting in a solid angle of 0.9 sr. Count-based fluorine elemental maps were acquired and were used to examine the ionomer distribution in the CLs relative to Pt. Cross-section MEAs were prepared by diamond-knife ultramicrotomy performed at ambient temperature, resulting in $\sim$75-nm thick MEA slices. The CL were embedded in epoxy before ultramicrotomy. The epoxy used was Araldite 6005 – MEAs were fully embedded and sliced at RT with a 35° diamond knife.

Results and Discussion

In this section, we report the measured dependence of R_{CL} on Pt loading, pressure, temperature, RH, reactant MW, I:C ratio, and primary particle loading, and segregate R_{CL} into sub-resistances. Since O$_2$ transport is more limiting than is H$_2$, we also compare qualitatively our results from H$_2$ limiting-current experiments against O$_2$ limiting-current literature data wherever possible. Similarity between O$_2$ and H$_2$ measurements demonstrates that we capture the characteristics of CL transport using H$_2$ in place of O$_2$.

Pt loading.—Cathode Pt loading is changed by increasing the thickness of the CL i.e., by adding more catalyst mass while the primary particle loading is held constant. Thus, a_v remains constant as explained above. The focusing factor, η, depends on the ionomer/gas interface area available per Pt particle. Since catalyst particles with same primary particle loading can be assumed to have the same Pt and ionomer distribution, we assert that η also remains constant in the examined samples. Thus, only the thickness of the CL differs among the examined samples.

Figure 4a displays measured R_{CL} using the H$_2$ pump for different Pt mass loadings on the WE. CL mass-transport resistance dominates
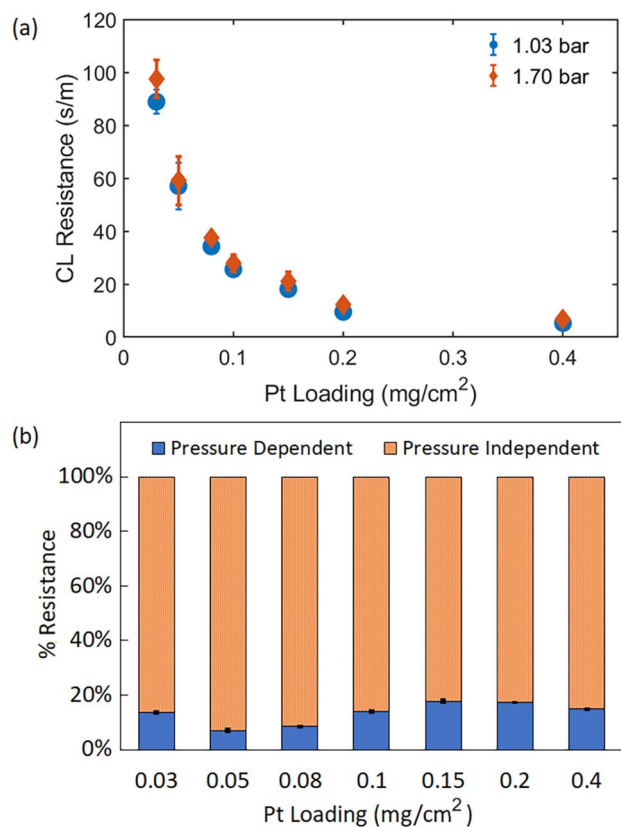
(a)

(b)

Figure 5. (a) R_{CL} at pressure 1.03 and 1.70 bar and T = 40°C, RH = 90%, showing identical trend with Pt loading. (b) Fraction of pressure dependent molecular transport resistance estimated at each loading. The contribution from pressure dependent resistance increases at high Pt-loadings.

R_{Total} at low Pt loadings.[12,16,17] The non-linear decrease in R_{CL} with increased Pt loading is in accord with literature.[12,16,17] By graphing R_{CL} versus $1/r_f$ in Figure 4b, a linear trend is observed, in agreement with O$_2$ limiting-current measurements.[12]

Upon comparing Figure 4b with Equation 17, the slope in Figure 4b yields $R_{Local}/\eta\gamma$. The linear dependence of R_{CL} on the inverse of the roughness factor, despite varying CL thickness, indicates that the through-plane CL resistance ($L/3D_{CL}^{eff}$) is small compared to the total local resistance ($R_{Local}/\eta\gamma\ r_f$). This is also supported by the fact that R_{CL} is significantly lower for high Pt-loading samples which have greater thickness and in agreement with literature.[17,54] The total local resistance is prominent at low loadings (i.e., at small r_f since it scales as $1/r_f$). This implies that the reactant gas concentration in the CL pores though the entire CL thickness remains relatively uniform.

Pressure.—R_{CL} was measured at pressures of 1.03 and 1.70 bar for different WE Pt loadings using the H$_2$-pump apparatus and interpreted by the GDL stacking method. As shown in Figure 5a, R_{CL} decreased strongly with increasing Pt-loading at both pressures. The pressure effect is weak over this range of pressure. From Equation 15, the fraction of pressure-dependent transport resistance is estimated at each loading and reported in Figure 5b. In accord with literature, the contribution to R_{CL} from pressure-dependent molecular transport resistance in CL ($L/3D_{H_2/Ar}^{Mol}$) is minimal at low loadings; other components dominate.[15]

Temperature and RH.—Figure 6 and Figure 7 display R_{CL} as functions of temperature and RH, respectively. Analogous to bulk-ionomer transport resistance[29] and R_{CL} reported in the literature using O$_2$ limiting-current measurements (O$_2$-R_{CL}),[15,36,55] H$_2$-R_{CL} measurements reported in Figure 6 also decrease drastically with increasing temperature, especially for low loadings. Since the local resistance
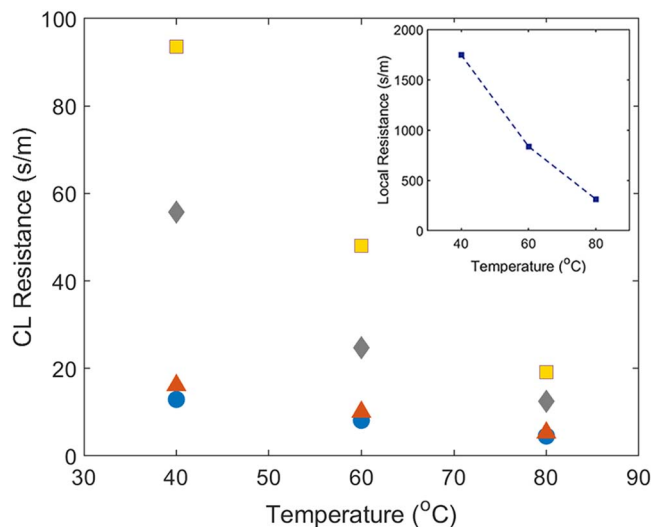

Figure 6. Temperature sensitivity of CL resistance for different WE Pt loadings at 1.035 bar, 90% RH. ● 0.4 mg/cm^2; ▲ 0.15 mg/cm^2; ◆ 0.08 mg/cm^2; ■ 0.03 mg/cm^2. The strong dependence of CL resistance on T is due to local resistance.

dominates at low loadings, we attribute the strong temperature sensitivity of R_{CL} to R_{Local} (η and γ are constant for the samples examined due to constant primary particle loading). This is in agreement with the findings of Kudo, et al.,[36] who observed both the transport resistance through the ionomer film and the interfacial resistance decrease with increasing temperature.

As shown in Figure 7, R_{CL} is much less sensitive to RH than to temperature with a slight decrease from 20 to 90% RH. Again, the RH dependence of R_{CL} is ascribed to R_{Local}, which does not change drastically with increasing RH. This contrasts to the sensitivity of O$_2$-R_{CL} measurements that demonstrate a strong RH dependence.[15,36,56] However, this difference is expected since H$_2$ transport through bulk ionomer also has weak humidity dependence compared to O$_2$ which has strong humidity dependence.[57,58] A detailed comparison of O$_2$ and H$_2$ mass-transport resistances in bulk ionomer as a function of temperature and RH is presented in SI.

The behavioral similarities between R_{CL} and bulk-ionomer transport resistance suggests that transport through the thin ionomer film is the main contributor to R_{CL}. Nonoyama et al.[15] came to a similar conclusion by studying the impact of operating conditions on O$_2$-R_{CL}.
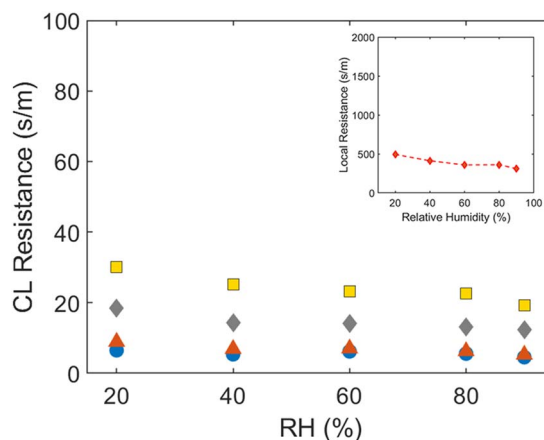

Figure 7. RH sensitivity of CL resistance for different WE Pt loadings at 1.035 bar, 80°C ● 0.4 mg/cm^2; ▲ 0.15 mg/cm^2; ◆ 0.08 mg/cm^2; ■ 0.03 mg/cm^2. Both CL resistance and local resistance show a weak dependence on RH.

However, the presence of interfacial resistance cannot be ruled out since it can also show a similar dependence on temperature and RH.[36]

If we ignore interfacial resistances and assume that ionomer thin-film thickness remains relatively constant with temperature, the temperature dependence of R_{Local} is solely determined by reactant permeability in the aqueous channels of the ionomer Π_{H_2/H_2O} (Equation 3), which is a product of reactant diffusivity and partition coefficient. The partition coefficient of reactant gases in water is assumed to have an Arrhenius temperature dependence.[46] Diffusion coefficient is also a function of temperature due to linear dependence on T and viscosity which has an Arrhenius temperature dependence (see Equation 11). Thus,

$$\Pi_{H_2/H_2O} = D_{H_2/H_2O}S_{H_2/H_2O} \propto Te^{\left(-\beta E_\mu/RT\right)}e^{\left(E_S/RT\right)} \quad [20]$$

where E_μ is the viscosity activation energy and E_S is partition coefficient activation energy. Upon taking the logarithm on both sides of Equation 20, one obtains

$$ln\ \Pi_{H_2/H_2O} \propto \frac{-1}{T}\left(\beta E_\mu - E_S\right) + ln\ T \quad [21]$$

Over small temperature ranges, $ln\ T$ is almost constant. Thus, the effective activation energy can be obtained from the slope of $ln\ R_{Local}$ vs $1/T$. Upon analyzing the temperature sensitivity data reported in Figure 6, an activation energy of ~39 ($\pm$ 17%) kJ/mol is calculated. This is higher than fully hydrated bulk-ionomer activation energy but close to the dry-ionomer activation energy,[46] which is consistent with the expected lower water content in CL thin-film ionomer,[59] once again suggesting that the ionomer thin-film is limiting, either due to its low permeability or due to presence of interfacial resistances.

Reactant MW.—Figure 5b confirms that pressure-independent resistance dominates R_{CL}, which includes Knudsen CL resistance, ionomer thin-film transport resistance, and interfacial resistances. Using the MW dependence of R_{CL} (see Equation 14), further insight can be gained. Figure 8a shows R_{CL} measured using H_2 and D_2 reactant gases as a function of Pt loading. Both H_2-R_{CL} and D_2-R_{CL} decrease with increasing Pt loading. H_2-R_{CL} is consistently lower than D_2-R_{CL} because of the lower MW of H_2 compared to D_2. The percentage contributions of MW-dependent transport resistances and MW-independent interfacial resistances calculated using Equation 14 are shown in Figure 8b for different Pt loadings. The non-zero percentage contribution from MW-independent resistance confirms the presence of interfacial resistances. Nevertheless, MW-dependent transport resistance dominates for all examined Pt loadings. In earlier sections, we showed that the overall contributions from through-plane resistance (which includes molecular and Knudsen transport resistance) to R_{CL} is minimal, especially at low loadings (e.g., see Figure 4b). Thus, the transport resistance through ionomer thin film seems to be the main source of large R_{CL} at low Pt loadings.

I:C ratio.—We have identified ionomer thin-film transport resistance, R_I, to be the largest contributor to R_{CL}. To validate this finding, we investigate R_{Local} as a function of ionomer mass to carbon mass (I:C) ratio. The assumption that the ionomer thin-film thickness increases linearly with ionomer content allows us to manipulate R_I while keeping the interfacial resistance constant.

Figure 9 shows $R_{Local}/\eta\gamma$ as a function of I:C ratio for both H_2 and D_2. $R_{Local}/\eta\gamma$ was estimated at each I:C ratio from the slope of R_{CL} versus $1/r_f$ for a range of different I:C ratios (see Figure S4 in SI). $R_{Local}/\eta\gamma$ increases linearly with I:C ratio. The increase of $R_{Local}/\eta\gamma$ with ionomer content in Figure 9 is attributed to increasing transport resistance due to thicker ionomer thin films. This figure also demonstrates that one should move toward lower I:C ratio to decrease the resistance, which should be valid up to the point that we lose connectivity and have high tortuosity for proton conductivity. By using I:C ratio as a proxy for δ and by comparing with Equations 3 and 17, the slope in Figure 9 is proportional to $1/\eta\gamma\Pi_{gas}$; the intercept gives the interfacial resistance component i.e., $(R_{I/Gas} + R_{Pt/I})/\eta\gamma$. Identical
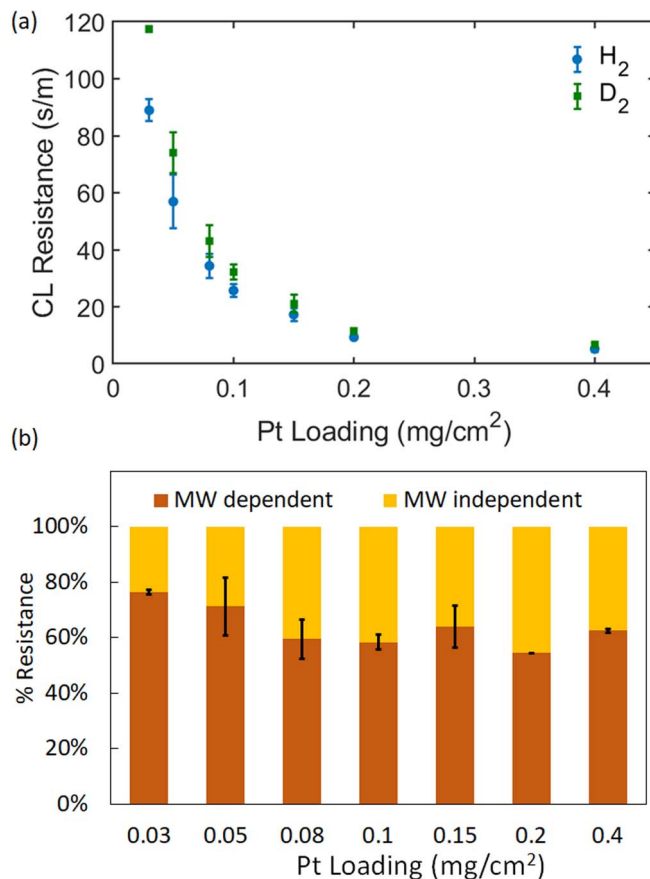

Figure 8. (a) CL resistance measured using H_2 and D_2 for different Pt loadings at 1.03 bar, 40°C and 90% RH, with H_2 exhibiting a lower resistance (b) Percentage contributions from MW dependent and independent components for H_2 resistance estimated from plot (a) data.

intercepts for H_2 and D_2 validate the assumption of MW-independent interfacial resistance. The ratio of slopes for D_2 to H_2 curves will be equal to the inverse of ratio of their ionomer thin film permeability i.e., Π_{H_2}/Π_{D_2} and calculated to 1.35 in close agreement with Equation 12.

Assuming uniform ionomer thickness with no ionomer penetration inside agglomerates, an estimate of the ionomer thin-film thickness for different I:C ratios is made. η is obtained from Figure 3 (for primary particle loading of 20 wt%) and the γ value approximated is 0.365[60] (i.e., $\eta\gamma \sim O(1)$). The thin-film H_2 permeability thus calculated is $\sim 5.64 \times 10^{-12}$ m²/s, which is an order of magnitude lower than
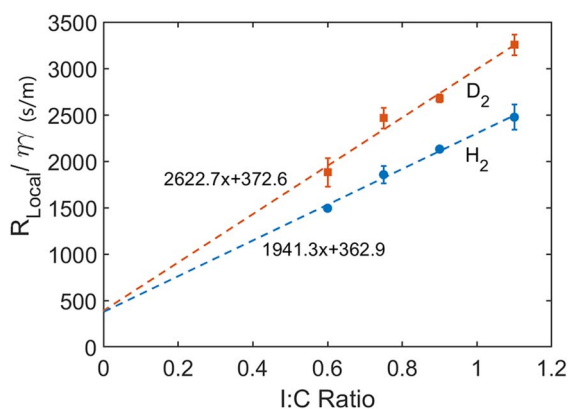

Figure 9. $R_{Local}/\eta\gamma$ for H_2 and D_2 at constant pressure of 1.03 bar, 40°C and 90% RH as a function of I:C ratio.
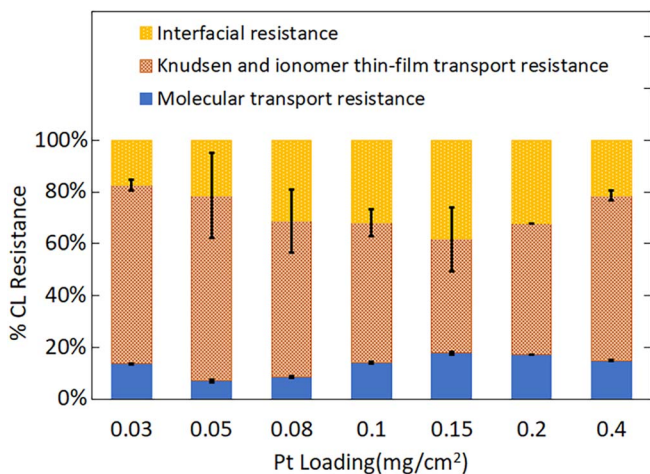
Figure 10. Contribution from different sub-resistances in CL for different Pt loadings at 1.03 bar pressure, 40°C, and 90% RH calculated from pressure and reactant MW dependence.

Table II. ECSA of samples with varying primary particle loading and total loading held constant at 0.05 mg/cm².

Primary Patricle Loading [wt%]	ECSA [cm²/cm²]
50	53.8
30	49.8
20	36.0

bulk-film permeability[29] and ionomer thin-film permeability measured from ex-situ experiments.[36] Detailed calculations for ionomer thin-film thickness including the values assumed for agglomerate radius and porosity are given in the SI.

The above analysis reveals that although R_{Local} is composed of both transport and interfacial components, the ionomer thin-film transport component dominates. Nevertheless, the individual elements of R_{CL} can be experimentally quantified using pressure and MW dependence of the component resistances. Figure 10 summarizes the relative contribution of component resistances for different Pt loadings, calculated using Equations 14 and 15. The pressure-dependent molecular-transport resistance is the smallest component accounting for < 20% of the total resistance and is likely due to a few large pores in the CL. The largest contribution is from the pressure-independent transport resistance, which includes transport through the ionomer thin film and through CL pores in the Knudsen regime and is between 50 to 70%. However, the through-plane CL resistance is minimal, and hence the pressure-independent transport resistance is attributed to the ionomer thin-film resistance. Lastly, the interfacial resistance that is both pressure and MW independent contributes ~20 to 35% of the total resistance.

These results contrast with the observations from ex-situ studies where the interfacial resistance was found to be the main cause of CL resistance.[33,37,61] However, one should note that the ex-situ experiments accurately control the ionomer thin-film thickness. In contrast, the CL structure is extremely heterogenous, with a distribution of ionomer thin-film thickness. The ionomer deposits on the carbon agglomerates in the ink in a very different environment compared to the usual ionomer-film casting methods, which could lead to specific morphological changes in the CL ionomer thin-films. In addition, the agglomerates have regions and Pt particles without any ionomer coating, which remain active due to proton conduction via condensed water. These active sites contribute to transport resistance, but not to interfacial resistance due to no direct ionomer contact. To highlight the impact of such heterogeneities in the CL structure, we next examine CL resistance as a function of primary particle loading.

Primary particle loading.—In previous sections, the total Pt mass loading was varied by changing the CL thickness, keeping the primary-particle loading constant. We now examine the impact of primary-particle loading on R_{CL}. Changing the primary-particle loading varies the distribution of Pt nanoparticles on the external agglomerate surface compared to the interior of the primary particles, with the fraction of Pt particles on the external surface increasing at high primary particle loadings.[60] Thus, both η and γ change because the number of Pt par-

ticles on the agglomerate external surface changes. η decreases with increasing primary particle loading, due to lower ionomer/gas interface area per Pt particle, while γ increases due to the higher fraction of Pt particles on the agglomerate external surface.[60]

Different primary-particle loadings (20, 30, and 50 wt-%) were studied while holding the total Pt loading constant at 0.05 mg/cm². HAADF-STEM images of the samples shown in Figure 11 demonstrate the heterogeneous CL structure with separate agglomerates formed by Pt-loaded HSC and bare KB particles and nonuniform ionomer distributions. The images also highlight that the ionomer preferentially deposits close to or on the agglomerates with Pt particles, possibly due to sulfonate-Pt interactions in the underlying casting inks.[62,63] However, this increased interaction is somewhat ameliorated by some of the ionomer interacting with the bare carbon agglomerates, which are inactive zones.

Figure 12a (Left) shows R_{CL} measured at fixed Pt loading of 0.05 mg/cm² at two different operating pressures (1.03 and 1.70 bar) and reactant MWs (H_2 and D_2). R_{CL} decreases significantly as the primary-particle Pt loading (weight percent) increases for each case. However, the samples also show a large deviation in ECSA (see Table II), which might be the cause of this trend. The deviations in ECSA are probably due to manual measurement error in the CL fabrication process. Since CL resistance is mostly contributed by local resistance which scales with inverse of ECSA, we normalize the resistances in Figure 12a (Left) with ECSA (referenced to 20wt% sample) to approximately correct for ECSA variation. This data is presented in Figure 12a (Right). Corrected CL resistance remains relatively constant and does not show any specific trend with primary particle loading. In contrast, the model predicts an increase in resistance at high primary particle loadings due to inverse dependence of R_{CL} on the factor ηγ, as η decreases significantly from 20 wt% to 50 wt% primary particle loading (see Figure 3) and γ increases slightly from 0.365 to 0.41.[60] Similar to predictions from model, Owejan, et al.[64] also observe an increase in resistance at high primary particle loadings while using Vulcan as carbon type. This highlights the effect of heterogeneities introduced due to use of different carbon types, such as non-uniform ionomer distribution. To investigate further, we estimate contributions from sub-resistances using ECSA-normalized resistances.

Equations 14 and 15 quantify the contributions from the various component resistances, presented in Figure 12b. As primary particle loading increases, an increase in the pressure-dependent resistance contribution can be rationalized by a change in the CL pore structure, porosity, and resultant increase of secondary pore sizes. This is also supported by the increased CL thickness of 50wt% sample (see SI for CL thickness measurements). The pressure-independent and MW-dependent transport resistances, which include Knudsen and ionomer thin-film transport resistances, decrease significantly as the primary particle loading increases while the interfacial resistance (which is both pressure and MW independent) displays an opposite trend.

The fraction of Pt particles on a carbon particle surface is known to increase with primary particle Pt loading. Thus, percentage interfacial-resistance increase is rationalized by an increased amount of exposed area for interaction between the Pt on the agglomerate surface and the ionomer, which is perhaps compounded by the fact that the strength of interaction is probably a function of proximity of interaction sites and ionomer moieties. This is also supported by the studies of Suzuki, et al.[33] and Jinnouchi, et al.,[37] where transport was examined through ionomer thin-film in direct contact with Pt surface. They found interfacial resistance as the dominant source of transport resistance.
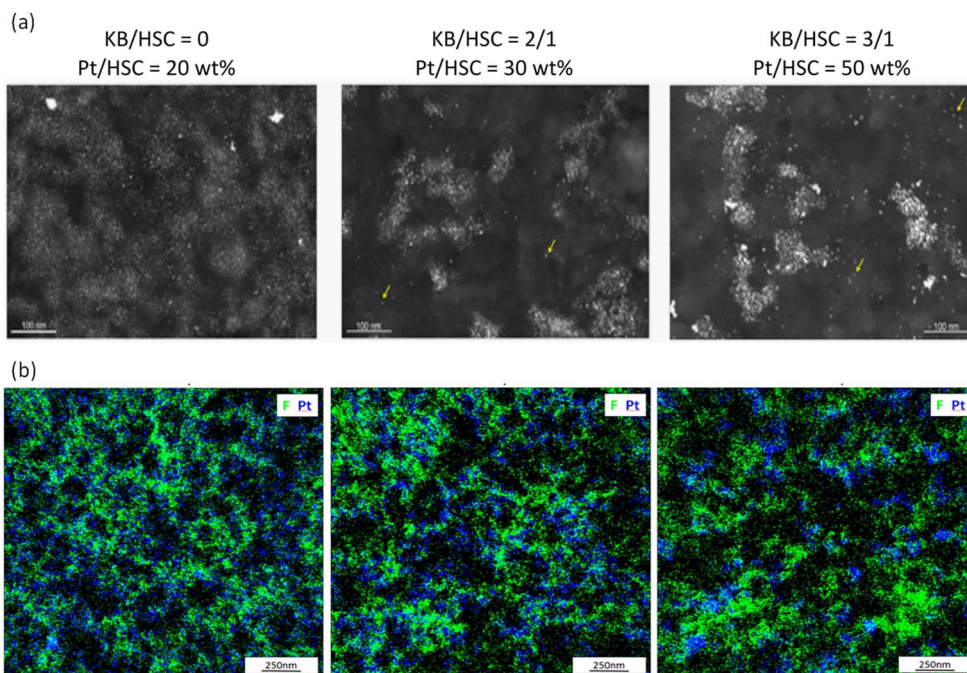
Figure 11. HAADF STEM imaging was performed to assess the morphology of the electrodes with different primary particle loading and ketjen black carbon dilution (a) Pt agglomerates are highlighted brightly while the ketjen black agglomerates are represented by gray contrast (b) The fluorine (ionomer) and Pt distribution mappings are represented in green and blue respectively for the three different samples. The heterogeneity in ionomer distribution increases for high primary particle loadings.
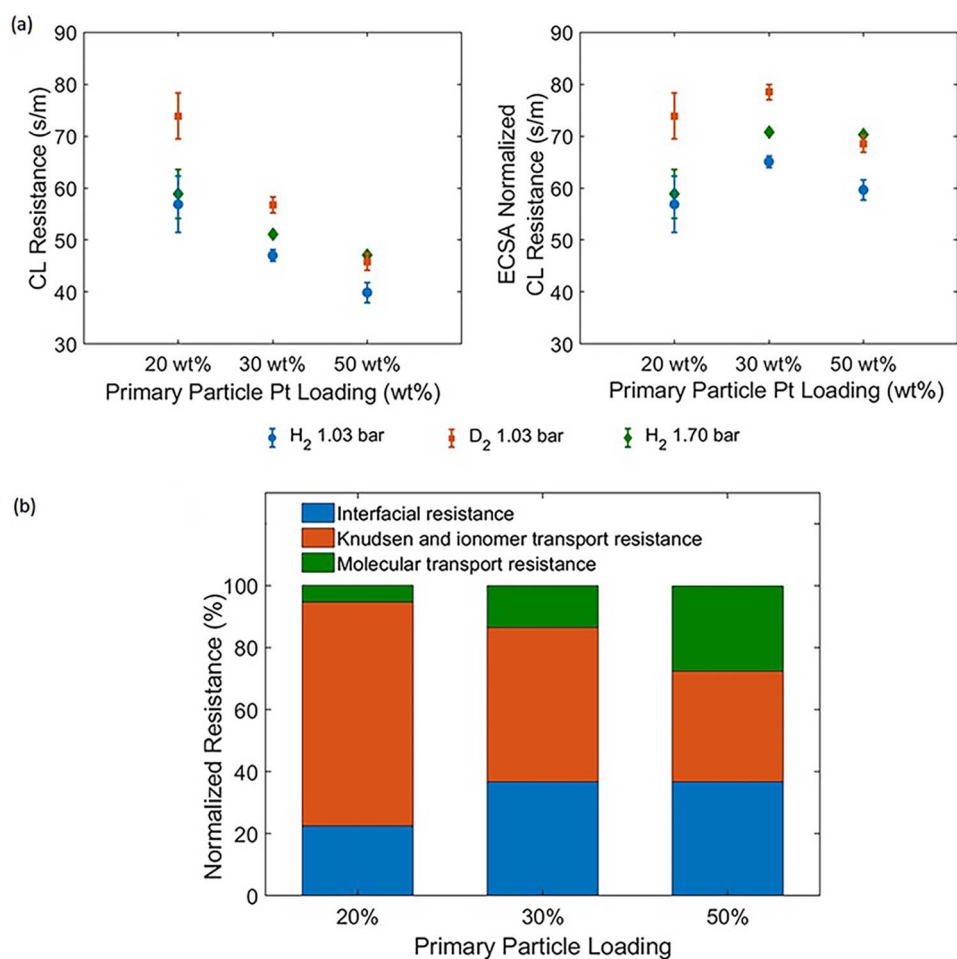

Figure 12. (a) Left: CL resistance measured for carbon supports with different primary particle loadings and constant total Pt loading of 0.05mg/cm^2 at 40°C and 90% RH; Right: CL resistance for different carbon supports corrected for ECSA (b) Breakdown of H$_2$ CL resistance from part (a) into Knudsen transport, interfacial and molecular diffusion components.

As the number of surface Pt particles decreases at low Pt loadings, the likelihood for reactant molecules to easily encounter a Pt particle and react decreases. In such situation, some of the Pt particles buried in the interior of carbon agglomerates might become active since the reactant molecules can now diffuse deeper into the agglomerate. These particles do not directly interact with Nafion, hence do not contribute to interfacial resistance. However, they do present a longer diffusional path length, thus increasing the transport resistance, as observed from our results. A similar idea was also proposed by Yarlagadda, et al.,[65] where they studied the impact of carbon type on CL resistance.

The observed decrease in pressure-independent/MW-dependent transport resistance contribution i.e, Knudsen and ionomer transport resistance can also be due to a non-uniform ionomer distribution. As highlighted in Figure 11, the ionomer seems to concentrate on or around Pt particles, while still coating the carbon particles to a certain extent. Samples with high Pt/C wt% have a higher fraction of Pt particles on their external surface compared to samples with low Pt/C wt%. However, the total ionomer content was maintained constant across all the samples. Thus, the same amount of ionomer interacts with a greater number of Pt particles in the case of high Pt/C wt% samples, which could potentially lead to a more uniform ionomer distribution and lower ionomer thin-film thickness on Pt particles compared to low Pt/C wt% samples. Another possible explanation is variations in agglomerate separation and structure, which is undoubtedly quite different. For example, for high primary particle loadings, it may be the case that the ionomer more successfully fills the agglomerate, thus leaving a thinner layer next to the outside Pt sites that are active during limiting-current conditions. Overall, the exact cause is not definitively known and future research is required to understand additional heterogeneities such as carbon types and amounts.

Conclusions

In this study, we present methods to isolate and quantify various sub-resistances of R_{CL} by exploiting their pressure and reactant-MW dependence using a H_2 limiting-current setup. Through systematic investigations, the results demonstrate that CL resistance is composed of transport and interfacial components. The transport resistance consists of through-plane resistance and ionomer thin-film transport resistance. The interfacial resistance is likely due to Pt-sulfonate interactions that are highlighted by the higher aggregation of ionomer around Pt particles as seen in HAADF-STEM imaging. However, further studies are required to verify this inference. Ionomer thin-film transport resistance along with interfacial resistance constitute the local resistance close to Pt particles.

The local resistance dominates with a small contribution from through-plane resistance. The pressure-independent transport resistance i.e., Knudsen transport resistance and ionomer thin-film transport resistance is the largest contributor to CL resistance. Since through-plane CL resistance, which includes Knudsen and molecular-transport resistance is shown to be minimal, the transport resistance through the ionomer thin-film or very local to the reaction site dominates. This finding is also verified from the impact of I:C ratio on local resistance. However, the relative contributions of interfacial and transport resistances depend on several CL design factors including CL porosity, Pt-mass loading, Pt-particle distribution, carbon type and ionomer content. This is highlighted by the influence of primary-particle Pt loading on component resistances where the interfacial resistance contribution increases significantly for high primary particle Pt loadings.

Acknowledgments

List of Symbols

a_v	Pt area on agglomerate external surface area per unit CL volume
A_{CL}	Geometric area of electrode
$C_{CL}(x)$	Local reactant concentration in CL pores
C_{avg}^{Feed}	Feed reactant concentration averaged over channel length
d_p	Pore diameter for Knudsen diffusion
D_{CL}^{eff}	Effective diffusion coefficient of reactant gas in CL
$D_{H_2/Ar}$	Reactant gas binary diffusivity in CL pores
$D_{H_2/Ar}^{Mol}$	Reactant gas molecular diffusion coefficient
$D_{H_2}^{Kn}$	Reactant gas Knudsen diffusion coefficient in CL pores
D_{A,H_2O}	Reactant gas A diffusion coefficient in water
$ECSA$	Total electrochemically active surface area of catalyst (m^2)
E_μ	Activation energy of water viscosity
E_S	Activation energy of gas partition coefficient in water
F	Faradays constant
$f_{Pressure}$	Fraction of pressure dependent transport resistance in total CL resistance
f_{MW}	Fraction of molecular weight dependent transport resistance in total CL resistance
I:C	Mass ratio of ionomer to carbon support
i_{lim}	Mass transport limited current density per unit CL geometric area
$i(x)$	Local mass transport limited current density per unit Pt area
L	CL thickness
MW_A	Molecular weight of species A
n	Moles of electrons transferred per mole reactant gas
N	Number of GDLs stacked in diffusion media
N_A	Avogardo's number
P	Total pressure
P_1/P_0	Pressure (P_1 and P_0 refer to two different operating pressures)
r_f	$ECSA/A_{CL}$ (m^2/m^2)
R_{Total}	Total mass transport resistance of cell (s/m)
R_{CL}	Mass transport resistance of CL (s/m)
R_{GDL}	Mass transport resistance of diffusion media (s/m)
R_{Foil}	Mass transport resistance of Cu foil (s/m)
R_{Local}	Local mass transport resistance associated with a single Pt particle
$R_{CL}^{D_2}/R_{CL}^{H_2}$	CL resistance with reactant gas D_2 or H_2
$R_{CL}^{P_1}/R_{CL}^{P_0}$	CL resistance at pressure P_1 or P_0
R_I	Mass transport resistance through inomer thin film
$R_{Pt/I}$	Resistance at Pt/ionomer interface due to sulfonate poisoning of catalyst
$R_{I/Gas}$	Gas dissolution resistance into the ionomer thin film
R	Ideal Gas constant
RH	Relative Humidity (%)
S_{A,H_2O}	Reactant gas A partition coefficient in water
T	Temperature °C
V_m	Molar volume at its normal boiling point

Greek

δ	Ionomer thin-film thickness
μ	Viscosity of the solvent
η	Focusing factor to correct for reactant flux (see SI)
α	$\sqrt{\eta a_v/R_{Local}D_{CL}}$

σ	Force constant from Lennard-Jones 6–12 potential
Λ^*	h/σ, where h is Planck's constant
Π_A	Permeability of species A through ionomer
Π_{A,H_2O}	Permeability of species A through water
β	$\sigma/(V_m/N_A)^{0.33}$
φ	Porous media porosity
τ	Porous media tortuosity
γ	Fraction of ECSA active at limiting current condition
ν	Species molecular volume (nm^3)

ORCID

Franz B. Spingler ⓘ https://orcid.org/0000-0002-6523-3986
Karren L. More ⓘ https://orcid.org/0000-0001-5223-9097
Adam Z. Weber ⓘ https://orcid.org/0000-0002-7749-1624

References

1. M. K. Debe, *Nature*, **486**, 43 (2012).
2. A. Kongkanand and M. F. Mathias, *J Phys Chem Lett*, **7**, 1127 (2016).
3. U. Beuscher, *Journal of the Electrochemical Society*, **153**, A1788 (2006).
4. D. A. Caulk and D. R. Baker, *J Electrochem Soc*, **157**, B1237 (2010).
5. J. Xie, D. L. Wood, K. L. More, P. Atanassov, and R. L. Borup, *J Electrochem Soc*, **152**, A1011 (2005).
6. K. More, R. Borup, and K. S. Reeves, *ECS Transactions*, **3**, 717 (2006).
7. M. Lopez-Haro, L. Guetaz, T. Printemps, A. Morin, S. Escribano, P. H. Jouneau, P. Bayle-Guillemaud, F. Chandezon, and G. Gebel, *Nat Commun*, **5**, 5229 (2014).
8. T. Morawietz, M. Handl, C. Oldani, K. A. Friedrich, and R. Hiesgen, *ACS Applied Materials & Interfaces*, **8**, 27044 (2016).
9. V. Berejnov, D. Susac, J. Stumper, and A. P. Hitchcock, *ECS Trans*, **50**, 361 (2012).
10. F. C. Cetinbas, R. K. Ahluwalia, N. Kariuki, V. De Andrade, D. Fongalland, L. Smith, J. Sharman, P. Ferreira, S. Rasouli, and D. J. Myers, *J Power Sources*, **344**, 62 (2017).
11. K. Karan, *Current Opinion in Electrochemistry*, **5**, 27 (2017).
12. T. A. Greszler, D. Caulk, and P. Sinha, *J Electrochem Soc*, **159**, F831 (2012).
13. T. Mashio, A. Ohma, S. Yamamoto, and K. Shinohaka, *ECS Transactions*, **11**, 529 (2007).
14. D. R. Baker, D. A. Caulk, K. C. Neyerlin, and M. W. Murphy, *Journal of the Electrochemical Society*, **156**, B991 (2009).
15. N. Nonoyama, S. Okazaki, A. Z. Weber, Y. Ikogi, and T. Yoshida, *J Electrochem Soc*, **158**, B416 (2011).
16. Y. Ono, A. Ohma, K. Shinohara, and K. Fushinobu, *J Electrochem Soc*, **160**, F779 (2013).
17. K. Sakai, K. Sato, T. Mashio, A. Ohma, K. Yamaguchi, and K. Shinohara, *ECS Transactions*, **25**, 1193 (2009).
18. W. Yoon and A. Z. Weber, *J. Electrochem Soc*, **158**, B1007 (2011).
19. A. Kongkanand, M. Dioguardi, C. Ji, and E. L. Thompson, *J Electrochem Soc*, **159**, F405 (2012).
20. S. A. Eastman, S. Kim, K. A. Page, B. Rowe, S. Kang, C. Soles, and K. Yager, *Macromolecules*, **45**, 7920−7930 (2012).
21. M. A. Modestino, D. K. Paul, S. Dishari, S. A. Petrina, F. I. Allen, M. A. Hickner, K. Karan, R. A. Segalman, and A. Z. Weber, *Macromolecules*, **46**, 867 (2013).
22. M. Bass, A. Berman, A. Singh, O. Konovalov, and V. Freger, *Macromolecules*, **44**, 2893 (2011).
23. M. Bass, A. Berman, A. Singh, O. Konovalov, and V. Freger, *J Phys Chem B*, **114**, 3784 (2010).
24. M. A. Modestino, A. Kusoglu, A. Hexemer, A. Z. Weber, and R. A. Segalman, *Macromolecules*, **45**, 4681 (2012).
25. K. A. Page, A. Kusoglu, C. M. Stafford, S. Kim, R. J. Kline, and A. Z. Weber, *Nano Lett*, **14**, 2299 (2014).
26. Z. Siroma, R. Kakitsubo, N. Fujiwara, T. Ioroi, S.-I. Yamazaki, and K. Yasuda, *J Power Sources*, **189**, 994 (2009).
27. D. K. Paul, R. McCreery, and K. Karan, *J Electrochem Soc*, **161**, F1395 (2014).
28. A. Kusoglu, T. J. Dursch, and A. Z. Weber, *Advanced Functional Materials*, **26**, 4961 (2016).
29. A. Kusoglu and A. Z. Weber, *Chem. Rev.*, **117**, 987 (2017).
30. T. J. Schmidt, U. A. Paulus, H. A. Gasteiger, and R. J. Behm, *J Electroanal Chem*, **508**, 41 (2001).
31. R. Subbaraman, D. Strmcnik, A. P. Paulikas, V. R. Stamenkovic, and N. M. Markovic, *Chemphyschem*, **11**, 2825 (2010).
32. K. Shinozaki, J. W. Zack, S. Pylypenko, B. S. Pivovar, and S. S. Kocha, *J Electrochem Soc*, **162**, F1384 (2015).
33. T. Suzuki, K. Kudo, and Y. Morimoto, *J Power Sources*, **222**, 379 (2013).
34. K. Kodama, A. Shinohara, N. Hasegawa, K. Shinozaki, R. Jinnouchi, T. Suzuki, T. Hatanaka, and Y. Morimoto, *J Electrochem Soc*, **161**, F649 (2014).
35. H. Liu, W. K. Epting, and S. Litster, *Langmuir*, **31**, 9853 (2015).
36. K. Kudo, R. Jinnouchi, and Y. Morimoto, *Electrochim Acta*, **209**, 682 (2016).
37. R. Jinnouchi, K. Kudo, N. Kitano, and Y. Morimoto, *Electrochim Acta*, **188**, 767 (2016).
38. A. Z. Weber and A. Kusoglu, *J Mater Chem A*, **2**, 17207 (2014).
39. F. B. Spingler, A. Phillips, T. Schuler, M. C. Tucker, and A. Z. Weber, *Int J Hydrogen Energ*, **42**, 13960 (2017).
40. A. T. S. Freiberg, M. C. Tucker, and A. Z. Weber, *Electrochemistry Communications*, **79**, 14 (2017).
41. A. Z. Weber, R. L. Borup, R. M. Darling, P. K. Das, T. J. Dursch, W. B. Gu, D. Harvey, A. Kusoglu, S. Litster, M. M. Mench, R. Mukundan, J. P. Owejan, J. G. Pharoah, M. Secanell, and I. V. Zenyuk, *J Electrochem Soc*, **161**, F1254 (2014).
42. W. Sun, B. A. Peppley, and K. Karan, *Electrochim Acta*, **50**, 3359 (2005).
43. A. Chowdhury, C. J. Radke, and A. Z. Weber, *ECS Trans*, **80**, 321 (2017).
44. W. Pollard and R. D. Present, *Physical Review*, **73**, 762 (1948).
45. R. B. Bird, W. E. Stewart, and E. N. Lightfoot, *Transport phenomena*, p. xii, J. Wiley, New York (2002).
46. M. Schalenbach, T. Hoefner, P. Paciok, M. Carmo, W. Lueke, and D. Stolten, *The Journal of Physical Chemistry C*, **119**, 25145 (2015).
47. J. Muccitelli and W. Y. Wen, *Journal of Solution Chemistry*, **7**, 257 (1978).
48. R. T. Ferrell and D. M. Himmelblau, *Journal of chemical and engineering data*, **12**, 111 (1967).
49. H. F. P. Knaap and J. J. M. Beenakker, *Physica*, **27**, 523 (1961).
50. G. S. Hwang and A. Z. Weber, *J Electrochem Soc*, **159**, F683 (2012).
51. F. Maillard, S. Pronkin, and E. R. Savinova, *Influence of size on the electrocatalytic activities of supported metal nanoparticles in fuel cell-related reactions*, John Wiley & Sons, Ltd. (2010).
52. J. Durst, A. Siebel, C. Simon, F. Hasche, J. Herranz, and H. A. Gasteiger, *Energy & Environmental Science*, **7**, 2255 (2014).
53. H. Iden and A. Ohma, *J Electroanal Chem*, **693**, 34 (2013).
54. M. Sabharwal, L. Pant, A. Putz, D. Susac, J. Jankovic, and M. Secanell, *Fuel Cells*, **16**, 734 (2016).
55. K. Sakai, K. Sato, T. Mashio, A. Ohma, K. Yamaguchi, and K. Shinohara, *ECS Trans*, **25**, 1193 (2009).
56. S. Shukla, D. Stanier, M. S. Saha, J. Stumper, and M. Secanell, *J Electrochem Soc*, **163**, F677 (2016).
57. K. Broka and P. Ekdunge, *J Appl Electrochem*, **27**, 117 (1997).
58. P. Gode, G. Lindbergh, and G. Sundholm, *J Electroanal Chem*, **518**, 115 (2002).
59. A. Kusoglu, A. Kwong, K. T. Clark, H. P. Gunterman, and A. Z. Weber, *J Electrochem Soc*, **159**, F530 (2012).
60. E. Padgett, N. Andrejevic, Z. Liu, A. Kongkanand, W. Gu, K. Moriyama, Y. Jiang, S. Kumaraguru, T. Moylan, R. Kukreja, and D. Muller, *J Electrochem Soc*, **165**, F173 (2018).
61. K. Kudo and Y. Morimoto, *ECS Trans*, **50**, 1487 (2013).
62. K. B. Hatzell, M. B. Dixit, S. A. Berlinger, and A. Z. Weber, *J Mater Chem A*, **5**, 20527 (2017).
63. S. A. Berlinger, B. D. McCloskey, and A. Z. Weber, *The Journal of Physical Chemistry B*, **122**, 7790 (2018).
64. J. P. Owejan, J. E. Owejan, and W. Gu, *J Electrochem Soc*, **160**, F824 (2013).
65. V. Yarlagadda, M. K. Carpenter, T. E. Moylan, R. S. Kukreja, R. Koestner, W. Gu, L. Thompson, and A. Kongkanand, *ACS Energy Letters*, **3**, 618 (2018).